Optimal two-layer directive microphone array with application in near-field acoustical holography

Mingsian R. Bai[a)]
Department of Power Mechanical Engineering, National Tsing-Hua University, 101, Section 2, Kuang-Fu Road, Hsinchu 30013, Taiwan

Chunkai Wang
Department of Mechanical Engineering, National Chiao-Tung University, 1001 Ta-Hsueh Road, Hsinchu 30013, Taiwan

Shen-Wei Juan
Department of Power Mechanical Engineering, National Tsing-Hua University, 101, Section 2, Kuang-Fu Road, Hsinchu 30013, Taiwan

(Received 2 September 2011; revised 9 April 2012; accepted 21 June 2012)

Conventional near-field acoustical holography (NAH) is generally based on the free-field assumption, which can cause errors when interfering sources are present in practical environments. To cope with this problem, previous research suggested a combined pressure-velocity approach for NAH that provides certain advantages to rejection of interferences. This paper revisits this idea in a broader context of optimal array design and examines the feasibility of using unidirectional microphones in each channel of the array such that the robustness of inverse reconstruction is enhanced against interfering sources. As indicated in the simulation, the numerical noise in finite difference estimation of particle velocity can nullify the advantage of the well-conditioned velocity-based reconstruction. In the proposed approach, the characteristics of each array channel consisting of two microphones are tailored by taking into account not only the directivity, but also the robustness against self-noise. An objective function based on directivity index and white noise gain is exploited in a linear quadratic optimization of a two-element end-fire array. The proposed optimal array is validated in conjunction with the equivalent source model (ESM) -based NAH through numerical simulations, with an interfering source positioned behind the array. The results have shown the directive optimal array has yielded improved quality of images in comparison with conventional approaches in the presence of an interfering source and sensor noise.
 [http://dx.doi.org/10.1121/1.4734238]

PACS number(s): 43.60.Fg, 43.60.Kx, 43.60.Lq, 43.60.Sx [EJS] Pages: 862–871

I. INTRODUCTION

In noise control engineering, identification of potential noise sources is a key step to noise diagnostics. Sound field reconstruction using microphone arrays has emerged as a useful tool for noise source identification by visualizing sound fields radiated by noise sources.[1–3] Microphone array techniques fall into two categories: Near-field acoustical holography (NAH)[4,5] and far-field beamforming.[6,7] Planar Fourier NAH was introduced in the 1980s by Williams and Maynard.[5] Since then, many alternative methods have been developed to cope with applications in more general and complicated scenarios.

In past years, many methods have been developed to extend the planar Fourier NAH for non-stationary noise[8] and arbitrarily shaped sources.[9–14] The Helmholtz equation least squares method suggested by Wu[15] used a representation of the sound field by using spherical harmonics. Another approach using different field representation named equivalent source methods (ESM) was also utilized for near-field source imaging. ESM represents the sound field radiated by sources with arbitrary geometry by using a distribution of discrete point sources.[16–19] A recent development of ESM-based NAH using multichannel inverse filtering was the near-field equivalent source imaging.[20–22] Comprehensive coverage of NAH can be found in the monograph by Williams[23] and a recent tutorial paper by Wu.[24]

Conventional NAH is generally based on the free-field assumption, which can cause errors when interfering sources are present in the test environments such as a live room and a car cabin. Recently, NAH based on measurement of sound pressure, particle velocity, and their combination were compared by Jacobsen and Liu[25] and Zhang *et al.*[26] Microflown sensors were employed to measure particle velocity in their study.[27] As they have demonstrated, the so-called combined *p-u* technique had better conditioned propagation matrices and thus attained better reconstruction quality, as compared with the pressure-based NAH. Along the same line, this paper aims to develop a NAH technique that is applicable in the scenarios where interfering sources are present. Instead of the costly microflown sensors, we examine the feasibility of using less expensive microphones and finite-difference method to estimate particle

a)Author to whom correspondence should be addressed. Electronic mail: msbai@pme.nthu.edu.tw

 0001-4966/2012/132(2)/862/10/$30.00

velocity. However, the finite-difference method is extremely susceptible to sensor mismatch and noise.[28,29] In order to enhance the robustness of measurement against interfering sources and noise in the application of NAH, this paper re-examine this issue in a broader context of optimal directional arrays. Specifically, each channel of the NAH array is designed with unidirectional characteristics, which is sensitive to sounds from only the front direction, in an attempt to suppress the interferences from the other directions especially from the rear side. In the approach, the directivity of each array channel consisting of two microphones is tailored by taking into account not only the directivity, but also the robustness against self-noise. Our methodology takes advantage of design criteria of end-fire two-microphone arrays,[30,31] in pursuit of the optimal balance between directional response and white noise gain for two microphones in each channel.[32] An objective function based on directivity index and white noise gain of a two-element end-fire array is exploited in the design of an optimal array. The proposed optimal array was investigated alongside the conventional *p-, u-, and pu*-based[26] arrays through a series of numerical simulations for ESM-based NAH, where an interfering source positioned at the rear of the array and self-noise are present.

II. THEORETICAL BACKGROUND

The source imaging method used in this work is the equivalent source method, which is a meshless collocation technique for discretizing integral equations.[30] In ESM, the sound field is represented by a distribution of virtual simple sources such as monopoles and dipoles. A linear system of matrix equations with source strengths as the unknowns can be obtained. The source strengths are calculated using Tikhonov regularization, which serves as the basis for reconstructing the acoustic variables on the source surface. The method using this procedure is referred to as the ESM-based NAH in the paper.[20,33]

A. The ESM-based NAH using p-u probes

A *pu*-based ESM suggested by Zhang *et al*. is reviewed as follows.[26] With ESM formulation the pressure vector $\mathbf{p}_a$ at the measurement positions can be related to the source strength vector $\mathbf{q}$ by

$$\mathbf{p}_a = j\rho_0 ck\mathbf{G}_{ap}\mathbf{q}, \tag{1}$$

where ρ_0 is the mass density of the medium, c is the speed of sound, $k=\omega/c$ is the wave number, ω is the angular frequency, and $\mathbf{G}_{ap}$ is a complex transfer matrix comprised of Green's functions $j=\sqrt{1}$,

$$\mathbf{G}_{ap} = \frac{1}{4\pi r}e^{-jkr}, \tag{2}$$

where r is the distance between the measurement point and the source

$$\hat{\mathbf{q}} = \frac{1}{j\rho_0 ck}\mathbf{G}_{ap}^{+}\mathbf{p}_a, \tag{3}$$

where $\hat{\mathbf{q}}$ is the estimated source strength vector and $\mathbf{G}_{ap}^{+}$ denotes the pseudo-inverse matrix of $\mathbf{G}_{ap}$. Once the source strength vector is calculated, the pressure and the normal velocity on the surface of the source can be reconstructed as

$$\mathbf{p}_s = j\rho_0 ck\mathbf{G}_{rp}\hat{\mathbf{q}}, \tag{4}$$

$$\mathbf{u}_{ns} = \mathbf{G}_{rv}\hat{\mathbf{q}}, \tag{5}$$

where $\mathbf{p}_s$ and $\mathbf{u}_{ns}$ are the reconstructed pressure and normal velocity vectors on the surface of the source, and $\mathbf{G}_{rp}$ and $\mathbf{G}_{rv}$ are the corresponding complex transfer matrices.

The NAH based on sound pressure measurement is called the *p*-based method in line with the terminology used in Ref. 26 Alternatively, particle velocity measurement can be used as the input to NAH. In this approach, the transfer relation reads

$$\mathbf{u}_{na} = \mathbf{G}_{av}\mathbf{q}, \tag{6}$$

where $\mathbf{u}_{na}$ is the normal particle velocity vector at the measurement positions and $\mathbf{G}_{av}$ is the corresponding transfer matrix. Once $\hat{\mathbf{q}}$ is determined, sound pressure and particle velocity can be reconstructed by using Eqs. (4) and (5). In Ref. 25 particle velocity measured by microflown sensors is used as the input to NAH. This approach is called the *u*-based method.

A modified approach referred to as the *pu*-based method, which combines pressure and velocity reconstructions is proposed in Ref. 26 The source estimated strength vector $\hat{\mathbf{q}}$ is obtained by the mean of source strengths reconstructed by pressure and particle velocity measurements,

$$\hat{\mathbf{q}} = \frac{1}{2}\left(\frac{1}{j\rho_0 ck}\mathbf{G}_{ap}^{+}\mathbf{p}_a + \mathbf{G}_{av}^{+}\mathbf{u}_a\right). \tag{7}$$

The *pu*-based method performs the *p*-based method and the *u*-based method when an interfering source is present at the rear of the array. In effect, the *pu*-based method is a cardioid microphone that has greater frontal gain than the rear, whereas the *p*-based method and the *u*-based method akin to an omni-microphone and a dipole microphone has symmetric patterns on two sides of the array.

B. Measurement of particle velocity

An alternative method of measuring particle velocity to the microflown sensor is through the finite difference approximation of the pressure gradient. By Euler's equation, particle velocity at the x direction is

$$u = \frac{j}{\rho_0\omega}\frac{\partial p}{\partial x}, \tag{8}$$

which is proportional to the pressure gradient. By using the two-point finite difference method, particle velocity can be approximated as

$$u = \frac{j}{\rho_0\omega}\frac{\partial p}{\partial x} \approx \frac{j}{\rho_0\omega}\frac{p_2 - p_1}{\Delta x}, \tag{9}$$

where p_1 and p_2 are pressure measurements at two adjacent points and Δx is the associated spacing. Alternatively, a higher order approximation can be obtained by using the four-point finite difference method.[34]

The four-point finite difference method presented in the paper is based on numerical differentiation. Given four discrete sample points (x_0, p_0), (x_1, p_1), (x_2, p_2), and (x_3, p_3), where x denotes the sensor position and p denotes the measured sound pressure, Lagrange interpolation enables the pressure field to be approximated by a third-order polynomial[35]

$$L(x) = \sum_{j=0}^{3} p_j \ell_j(x), \tag{10}$$

where

$$\ell_j(x) = \prod_{\substack{0 \le m < 3 \\ m \ne j}} \frac{x - x_m}{x_j - x_m} \tag{11}$$

and $x_0 = 0$, $x_1 = \Delta x$, $x_2 = 2\Delta x$, and $x_3 = 3\Delta x$ with Δx being the interelement spacing. As such, the expression of particle velocity u at the center $(x_c = 1.5\Delta x)$ can be derived in light of the momentum equation,

$$u = \frac{j}{\rho_0 \omega} \frac{\partial p}{\partial x} \approx \frac{j}{\rho_0 \omega} \frac{p_0 - 27p_1 + 27p_2 - p_3}{24\Delta x}. \tag{12}$$

Despite the simplicity, the finite difference approximation is prone to numerical noise inflicted by the subtraction operation. To see this effect, a noise analysis of the finite difference approximation is carried out for velocity reconstructed suing the ESM-based NAH on a planar rectangular piston. For clean signals, the relative error of velocity obtained using NAH with particle velocity input approximated by the finite difference method is lower than that of the velocity obtained using NAH with pressure input, as has been demonstrated in Ref. 25. However, if the pressure signals picked up by microphones are corrupted by self-noise with 40 dB signal-to-noise ratio (SNR), the error of the finite difference approximation is considerably higher than the results of the NAH with pressure input and even exceeds 300% below 500 Hz, as shown in Fig. 1. Phase mismatch leads to larger error than magnitude mismatch, as shown in Fig. 2. It is this drawback of the finite difference approximation that motivates the development of the optimal two-microphone directive end-fire array. In the following, we use only the two-point approach in the numerical verification mainly because the results have shown that the four-point approach was unable to improve the velocity estimation accuracy significantly over the two-point approach, which was already very sensitive to the self-noise and mismatch of microphones.

C. Differential microphone array

In fact, the aforementioned *u*- and *pu*-based methods are closely connected to first-order differential microphone array (DMA). To capture only the essence of DMA, we assume a plane wave field for simplicity,

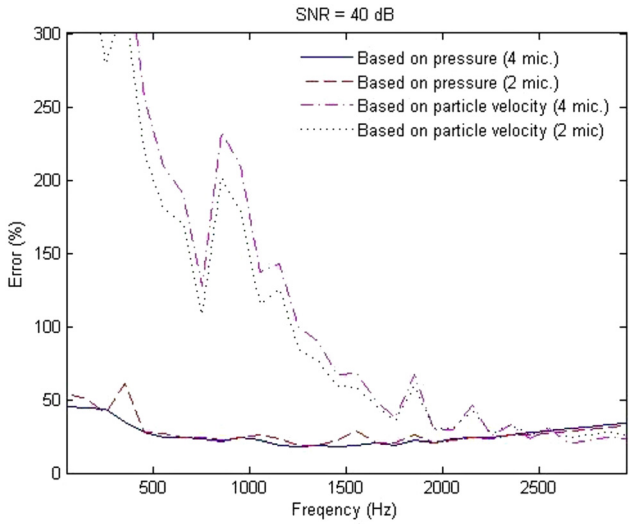

FIG. 1. (Color online) The relative error (%) of particle velocity reconstructed using ESM-based NAH with 40 dB SNR white noise.

$$p_i(\mathbf{r}) = Ae^{-jkr\cos\theta}, \tag{13}$$

where A is amplitude, $\mathbf{r}$ is position vector, $r = |\mathbf{r}|$, θ is the subtending angle between $\mathbf{r}$ and the wave vector of the plane wave. According to the Euler equation, the particle velocity at the $\mathbf{r}$ direction can be expressed by taking the pressure gradient of the incident plane wave,

$$\begin{aligned} u_r(\mathbf{r}) &= \frac{j}{\rho_0 \omega} \frac{\partial p_i}{\partial r}(\mathbf{r}) = \frac{j}{\rho_0 \omega}[-jk\cos\theta\, p_i(\mathbf{r})] \\ &= \frac{1}{\rho_0 c}\cos\theta\, p_i(\mathbf{r}), \end{aligned} \tag{14}$$

which displays a dipole characteristic. If we equalize Eq. (14) with $\rho_0 c$ and combine the pressure gradient with the pressure measurement, we obtain

$$p_D(\mathbf{r}) = \frac{1}{2} p_i(\mathbf{r}) + \frac{\rho_0 c}{2} u_r(\mathbf{r}) = (0.5 + 0.5\cos\theta) p_i(\mathbf{r}), \tag{15}$$

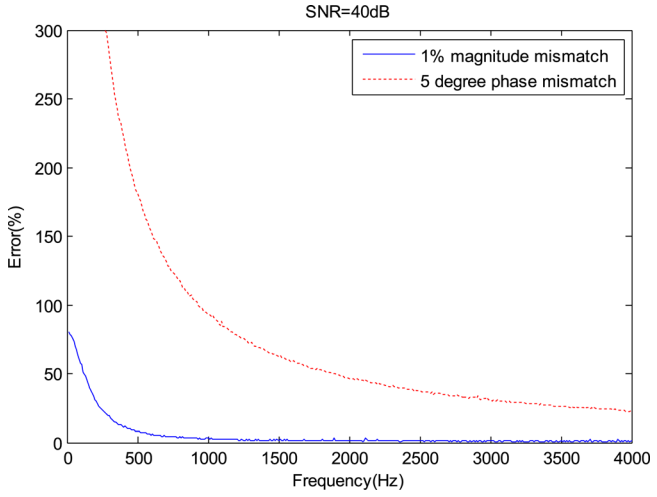

FIG. 2. (Color online) The relative error (%) of particle velocity reconstructed using ESM-based NAH with 5° phase mismatch and 1% magnitude mismatch at 40 dB SNR. The input signal is band-limited white noise.

which displays a cardioid characteristic. The frequency-independent directivity patterns explain why the *pu*-based approach outperforms the *u* based approach in rejecting interfering sources from the rear of the array in the results of Zhang *et al*.[26]

We can generalize the preceding argument to a broader context by linearly combining a pressure microphone (monopole) and an equalized gradient microphone (dipole) with a weighting parameter α_1 to form a first-order DMA. That is,

$$p_D(\mathbf{r}) = \alpha_1 p_m(\mathbf{r}) + (1-\alpha_1)\frac{jc}{\omega}\frac{\partial p}{\partial n}(\mathbf{r}) = [\alpha_1 + (1-\alpha_1)\cos\theta]p_i(\mathbf{r}), \tag{16}$$

where $(\partial p/\partial n)(\mathbf{r})$ is the pressure gradient and $\mathbf{n}$ is the unit vector pointing to the dipole direction.

Therefore, the associated directivity function is

$$H(\omega,\theta) = \alpha_1 + (1-\alpha_1)\cos\theta. \tag{17}$$

With some manipulations, it can be shown, with $\alpha_1 = 0.25$, that the first order that maximizes directivity index (DI) is the hypercardioid array. A hypercardioid attains the maximum DI 6.0 dB and the 105° beamwidth (3 dB).

Despite the frequency-independent directivity, prior research has shown that DMAs are extremely sensitive to mismatch and noise of sensors when the spacing is small. A sensitivity function for an *n*th-order dipole case was derived[27]

$$K_D \approx \frac{n+1}{(kd)^n}, \tag{18}$$

where $n = 1$ is the order of the DMA, d is the microphone spacing, and $kd \ll 1$. Therefore, it is generally impractical, if not impossible, to implement a high-order DMA with unduly small spacing due to mismatch and noise of transducers.

D. Optimal two-microphone directive end-fire array

The forging design approach focuses on only the directional response of the array, which can likely result in noise-susceptible arrays. The design of array systems is all about achieving the optimum tradeoff between directivity versus white noise gain for the application in question. In this section, we shall examine the issue from a more general perspective. Consider an M-element array with coefficient vector **w.** Two performance measures are based on the *array gain* (ratio of the SNR at the array output called the *output SNR* to the SNR observed at a single element called the *input SNR*) subject to different types of noise.[32]

The first performance measure, DI, is the array gain due to *isotropic acoustical noise* as follows:

$$DI = 10\log\frac{|\mathbf{w}^H\mathbf{a}|^2}{\mathbf{w}^H\mathbf{R}_{vv}\mathbf{w}}, \tag{19}$$

where $\mathbf{R}_{vv}$ denoted an isotropic noise coherence matrix defined as

$$\{\mathbf{R}_{vv}\}_{mn} = \frac{\sin[(m-n)kd]}{(m-n)kd}, \qquad m,n = 1,2,\ldots,M. \tag{20}$$

The second performance measure, white noise gain (WNG), is due to *spatially uncorrelated noise*, such as sensor's self-noise as in our case,

$$WNG = 10\log\frac{|\mathbf{w}^H\mathbf{a}|^2}{\mathbf{w}^H\mathbf{w}}, \tag{21}$$

which can be regarded as a measure for robustness against sensor noise. Further, if we impose the so-called *distortionless constraint*

$$|\mathbf{w}^H\mathbf{a}| = 1, \tag{22}$$

the WNG of array reduces to

$$WNG = \frac{|\mathbf{w}^H\mathbf{a}|^2}{\mathbf{w}^H\mathbf{w}} = \frac{1}{\|\mathbf{w}\|_2^2}. \tag{23}$$

That is, the lower the WNG, the larger the norm of array coefficient vector.

Array design that attains high DI normally comes at the price of low WNG. For instance, the "delay and subtract" action of a DMA results in substantial cancellation of signals, especially in the low frequency range. Therefore, there is a tradeoff between the gain in directivity (DI) with improved sidelobe behavior and loss in robustness against self-noise (WNG), or equivalently, increase in the norm of array coefficients. As an intuitively appealing approach, we here aim for an optimal compromise between directivity and robustness by weighting the reciprocals of the DI and WNG of the array, in light of the aforementioned linear quadratic optimization (with dB definition suppressed).

$$\begin{aligned}\min_{\mathbf{w}}\left(\frac{1}{DI}+\varepsilon\frac{1}{WNG}\right) &= \min_{\mathbf{w}}\left[\frac{\mathbf{w}^H\mathbf{R}_{vv}\mathbf{w}}{\mathbf{w}^H\mathbf{a}(\theta_0)\mathbf{a}^H(\theta_0)\mathbf{w}} + \varepsilon\frac{\mathbf{w}^H\mathbf{w}}{\mathbf{w}^H\mathbf{a}(\theta_0)\mathbf{a}^H(\theta_0)\mathbf{w}}\right]\\ &= \min_{\mathbf{w}}\left[\frac{\mathbf{w}^H(\mathbf{R}_{vv}+\varepsilon\mathbf{I})\mathbf{w}}{\mathbf{w}^H\mathbf{a}(\theta_0)\mathbf{a}^H(\theta_0)\mathbf{w}}\right]\\ &= \max_{\mathbf{w}}\left[\frac{\mathbf{w}^H\mathbf{a}(\theta_0)\mathbf{a}^H(\theta_0)\mathbf{w}}{\mathbf{w}^H(\mathbf{R}_{vv}+\varepsilon\mathbf{I})\mathbf{w}}\right],\end{aligned} \tag{24}$$

assuming axisymmetry and $0 < \varepsilon < 1$ is a parameter that weights DI versus WNG. In our case of a two-element end-fire array ($\theta_0 = 0°$),

$$\mathbf{a}(\theta,\ \phi) = [1 \quad e^{ijd\cos\theta}]^T, \tag{25}$$

$$\mathbf{R}_{vv} = \begin{bmatrix} 1 & \frac{\sin kd}{kd} \\ \frac{\sin kd}{kd} & 1 \end{bmatrix}. \tag{26}$$

Solving the problem of Eq. (17) leads to the following optimal solution of array coefficients:

$$\mathbf{w}_{\mathrm{SD}} = \frac{(\mathbf{R}_{vv} + \varepsilon\mathbf{I})^{-1}\mathbf{a}(\theta_0)}{\mathbf{a}^H(\theta_0)(\mathbf{R}_{vv} + \varepsilon\mathbf{I})^{-1}\mathbf{a}(\theta_0)}. \tag{27}$$

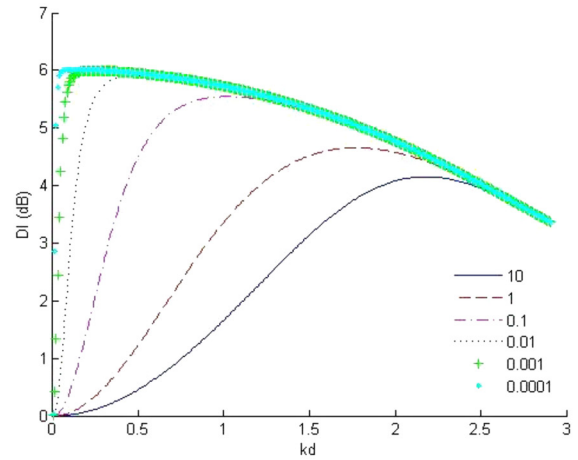

(a)

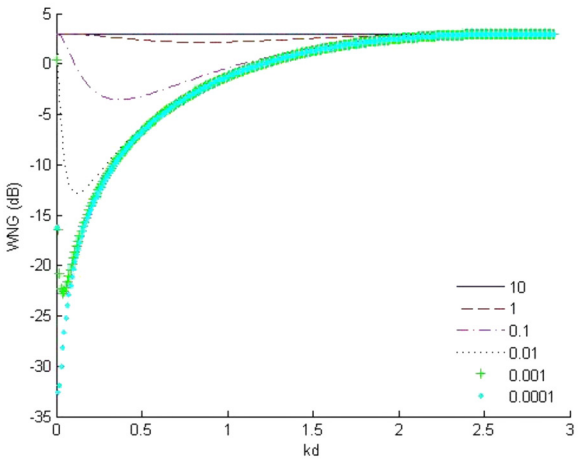

(b)

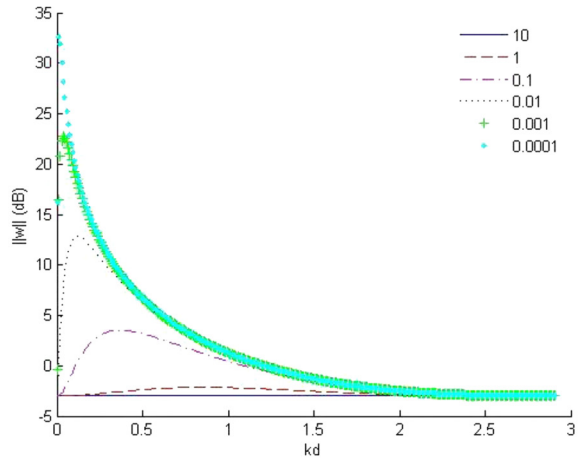

(c)

FIG. 3. (Color online) Performance index curves of a two-element optimal array, plotted with the weighting parameter $\varepsilon = 0.0001$–10. (a) DI, (b) WNG, and (c) coefficient norm.

Incidentally, this result turns out to be identical to the superdirective array obtained by Bitzer and Simmer.[31] The optimal trade-off between DI and WNG (or coefficient norm) is the physical insight underlying the action of regularization in the context of array design. By varying the parameter ε between 0 and ∞, we have an array at two extremes corresponding to the superdirective array with maximum DI and the delay-and-sum beamformer with maximum WNG. Figure 3 shows DI, WNG, and coefficient norm of a two-element end-fire array with ε raging from 0.0001 to 10. The larger the parameter ε, the more robust is the array at some expense of directivity. In this work, we choose $\varepsilon = 0.01$ for the array design in numerical simulations, such that the array not only rejects interfering sources but also increases the robustness against sensor noise and mismatch.

E. Performance comparison of two-microphone arrays

In the section, we selectively compare the performance of four designs of two-microphone directive arrays on a one-channel basis. The array is of the "filter-and-sum" architecture, as illustrated in Fig. 4.

The first array is the *p*-based array in which sound pressure is estimated by the mean of the pressure data picked up by two microphones in each channel,

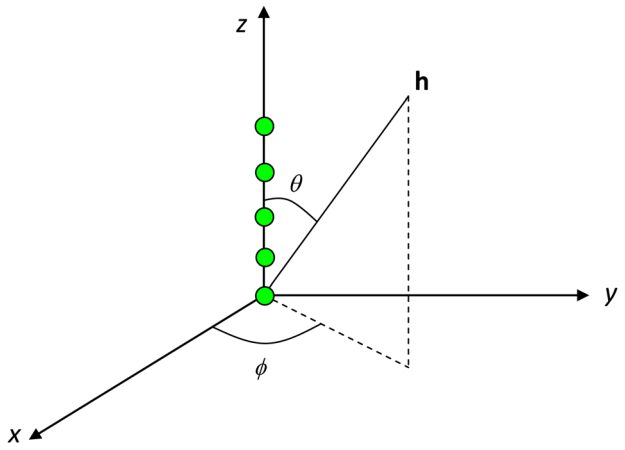

(a)

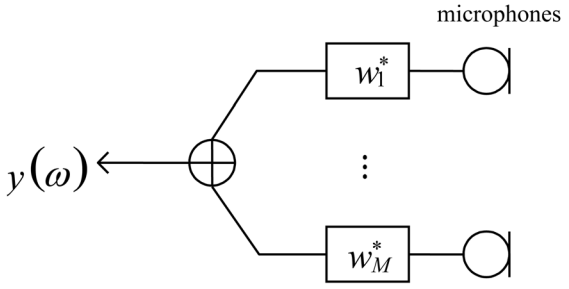

(b)

FIG. 4. (Color online) Microphone array architecture. (a) The coordinate system and (b) the block diagram of a filter and sum array.

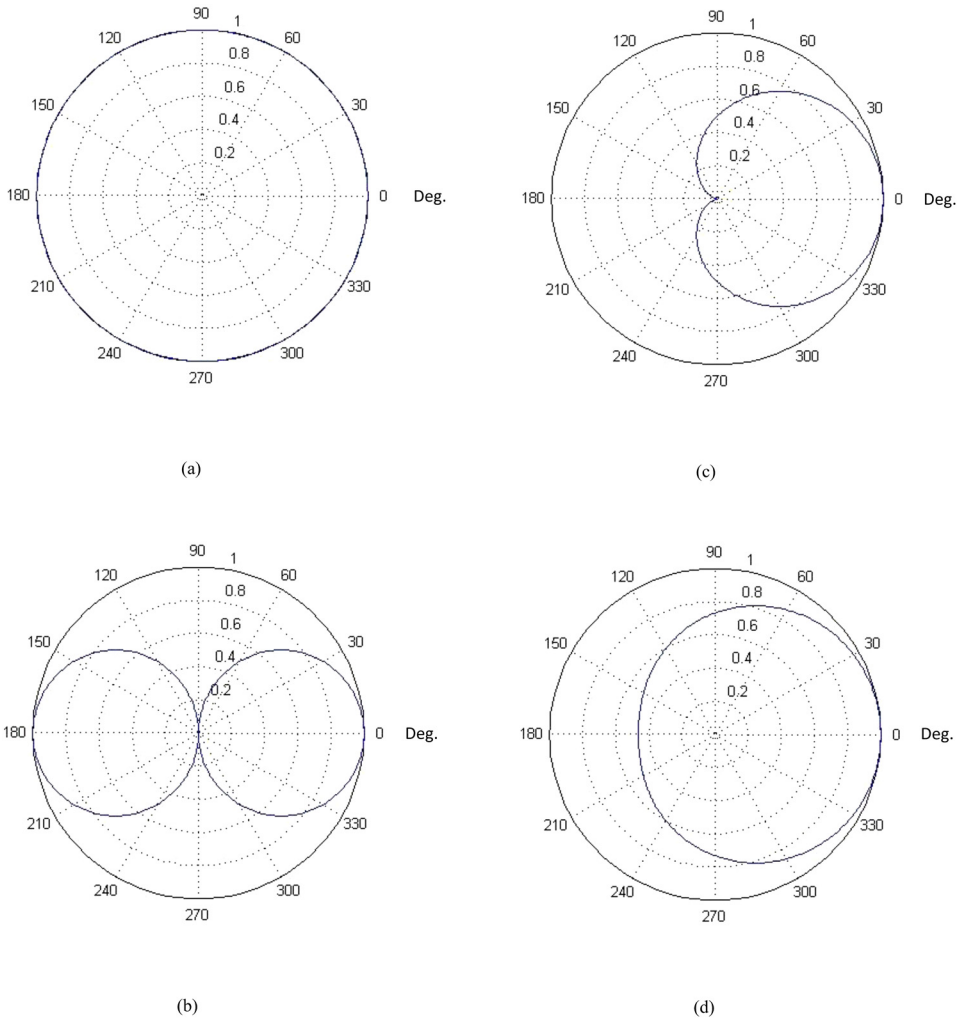

FIG. 5. (Color online) The polar plots of directivity pattern at 1 kHz of (a) *p*-based array, (b) *u*-based array, (c) *pu*-based array, and (d) optimal array.

$$p(\omega) = \frac{p_1(\omega) + p_2(\omega)}{2}, \tag{28}$$

where $p_1(\omega)$ and $p_2(\omega)$ are pressure data picked up by the front microphone and the back microphone in a channel of the array. The second array is the *u*-based array in which particle velocity is estimated by the aforementioned two-point finite difference method. The third array is the *pu*-based array in which sound pressure and particle velocity are estimated as the previous two approaches. The fourth array is the optimal array designed using the preceding linear quadratic approach with weighting parameter $\varepsilon = 0.01$. Figure 5 shows the directional channel responses of all arrays at 1 kHz. As expected, the *p*-based array is nearly omni-directional; the *u*-based array exhibits the figure-eight pattern of a dipole; the *pu*-based array exhibits the pattern of a cardioid. All but the *p*-based array have more frontal pickup than rear pickup. Unlike the other three arrays, however, the directional response of the optimal array is frequency-dependent, as depicted in Fig. 6. The optimal array's frontal pickup is greater than that of the rear above ~500 Hz. Inspection of the directivity patterns of the above-mentioned arrays, we may expect that, except for the *p*-based array, the three other arrays are capable of rejecting the interfering sources, especially those from the rear of the array.

However, directivity is not the only design factor one needs to take into consideration. Figure 7 shows the DI, WNG, and the coefficient norm, plotted versus the dimensionless parameter *kd* of each array. The *p*-based array is omni-directional (DI = 0 dB). Both the *u*-based array and the *pu*-based array achieved identical DI = 4.8 dB. DI of the

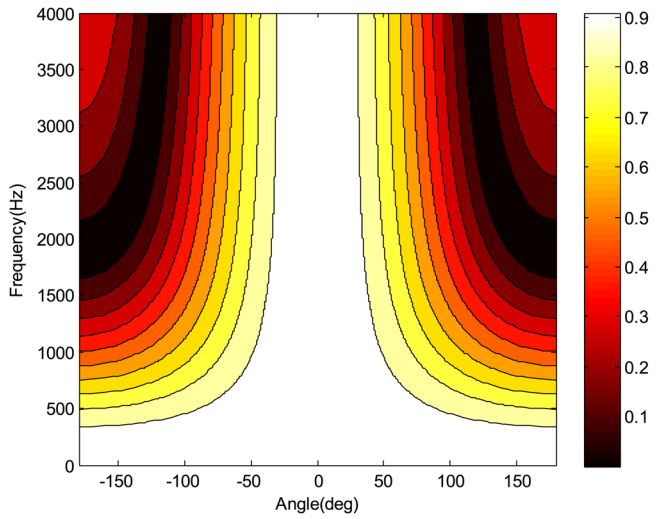

FIG. 6. (Color online) The directivity pattern of the optimal array, plotted versus angle and frequency. The color bar is expressed in linear scale.

optimal array increases monotonically with frequency. We can clearly see the conflicting trends in DI, WNG, and coefficient norm for all array designs. As will be shown in the following presentation, the design in pursuit of a single objective generally results in degradation, or even failure, in either performance or robustness of NAH.

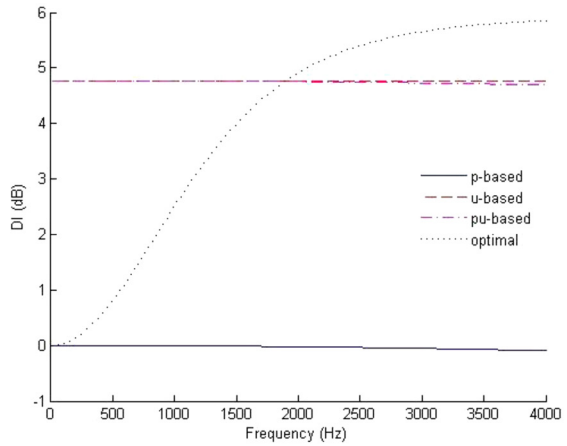

(a)

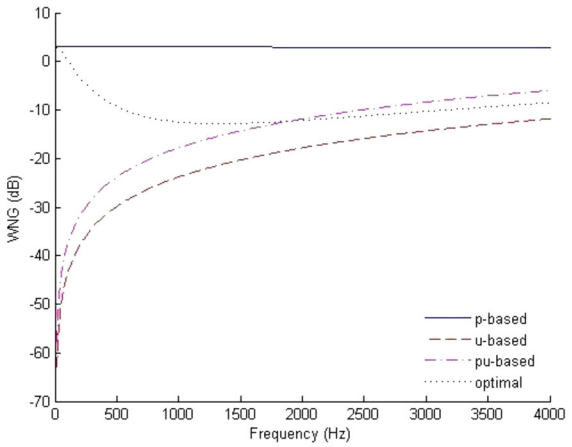

(b)

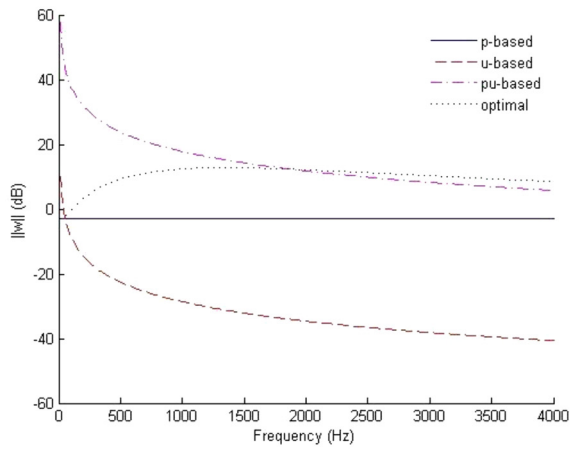

(c)

FIG. 7. (Color online) Performance index curves of four two-element arrays used in the simulated. (a) DI, (b) WNG, and (c) coefficient norm.

III. NUMERICAL AND EXPERIMENTAL INVESTIGATIONS

In order to examine the feasibility of the directive two-microphone end-fire array in the application to NAH, numerical simulations are undertaken to examine the effects of interference and self-noise on the quality of image reconstructed by the ESM-based NAH. Figure 8 illustrates the arrangement of the numerical simulation. The reconstruction plane is located at $z=0$ m and interpolated to 200×200 grid points. The microphone arrays are located at $z=0.05$ m and distributed with the same 6×5 grid points with lattice spacing 0.05 m (0.146λ at $f=1$ kHz). The distance of reconstruction is also 0.05 m. The equivalent source plane is located at $z=-0.025$ m and distributed with the same 6×5 grid points. Therefore, the retreat distance is 0.073λ at $f=1$ kHz. The source plane is located at $z=0$ m and distributed with 6×5 grid points. In the NAH simulation, we are targeted at two point sources located at (0.15 m, 0.05 m, −0.025 m) and (0.05 m, 0.2 m, −0.025 m), respectively. Random noise band-limited to the frequency 1 kHz serves as the target source signal. Another point source is placed at (0.1 m, 0.125 m, 0.15 m), which is 0.1 m behind the array, to interfere with the microphone measurement. In the NAH reconstruction, the sampling rate is selected to be 8 kHz. A low pass filter with cutoff frequency 1 kHz is used for anti-aliasing. Signal picked up by each microphone channel is corrupted with uncorrelated random noise such that the SNR is 40 dB.

Figure 9 summarizes the velocity reconstructed by using the ESM-based NAH with various inputs obtained using the *p*-based, the *u*-based array, the *pu*-based array, and the optimal array. The velocity reconstructed by the *p*-based array in Fig. 9(a) shows two target sources. The quality of velocity reconstructed by the *u*-based array in Fig. 9(b) is worse than that of the preceding *p*-based result. The velocity reconstructed by the *pu*-based array in Fig. 9(c) shows two target sources, the reconstruction quality is between the *p*-based and *u*-based arrays. Finally, the quality of velocity

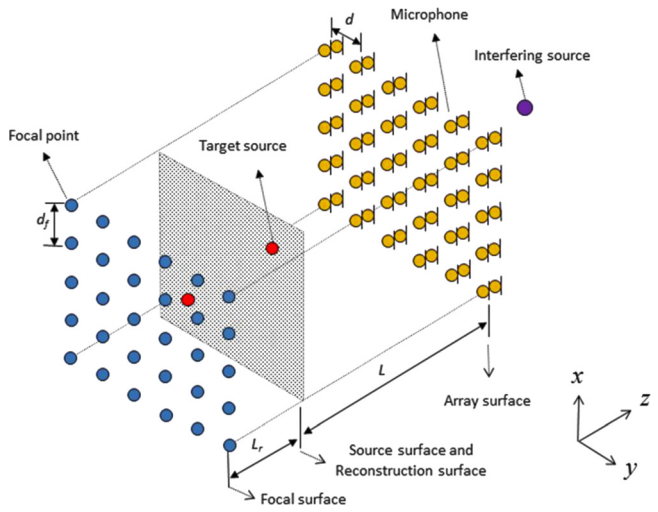

FIG. 8. (Color online) The arrangement of NAH system, where d is the microphone spacing, L is the distance of reconstruction (DOR), L_r is retreated distance, and d_f is the spacing of focus point.

reconstructed by the optimal array in Fig. 9(d) is similar to the velocity reconstructed by the *pu*-based array. The results have shown that the optimal array helps improve the robustness against interfering sources, as well as uncorrelated self-noise, which is an appealing feature in particular when NAH is applied in real-world scenarios where interferences are present.

In addition to numerical simulations, experimental investigations are conducted in the revised paper to further manifest that the optimal tradeoff between DI and WNG is indeed the key to the success of practical implementation of the directional NAH. All settings including the positions of target sources and the interferer are identical to those used in the simulation. A uniform rectangular array (20 cm × 25 cm) was constructed for the experimental verification of the proposed approach, as shown in Fig. 10(a). Each channel was fitted with two microelectromechanical systems (MEMS) microphones [Knowles SPM0410HR5H-PB (Knowles Electronics, Itasca, IL)], which totals 30×2 channels in the array. Three small loudspeakers with uncorrelated 6 s segments of white noise input were used to simulate two target sources and one rear interferer, as shown in Fig. 10(b). Data acquisition and processing were implemented on the platform of LABVIEW and PXI system of National Instruments® (Austin, TX) with 8 kHz sampling rate. The experiment was performed in a 6 m × 3 m × 3 m anechoic room.

The image reconstructed by the *p*-based method in Fig. 10(c) showed two target sources, with an undesired shadow at the lower left due to the interference. The quality of image reconstructed by the *u*-based method in Fig. 10(d) was considerably worse than that of the preceding *p*-based result, where the target sources were completely missed. Although the image reconstructed by the *pu*-based method in Fig. 10(e) showed two target sources, the source on the lower right was markedly displaced. Last, the quality of image reconstructed by the proposed optimal directional array in Fig. 10(f) is significantly better than all preceding results. The two target sources are clearly visible and the impact due to interference is virtually negligible.

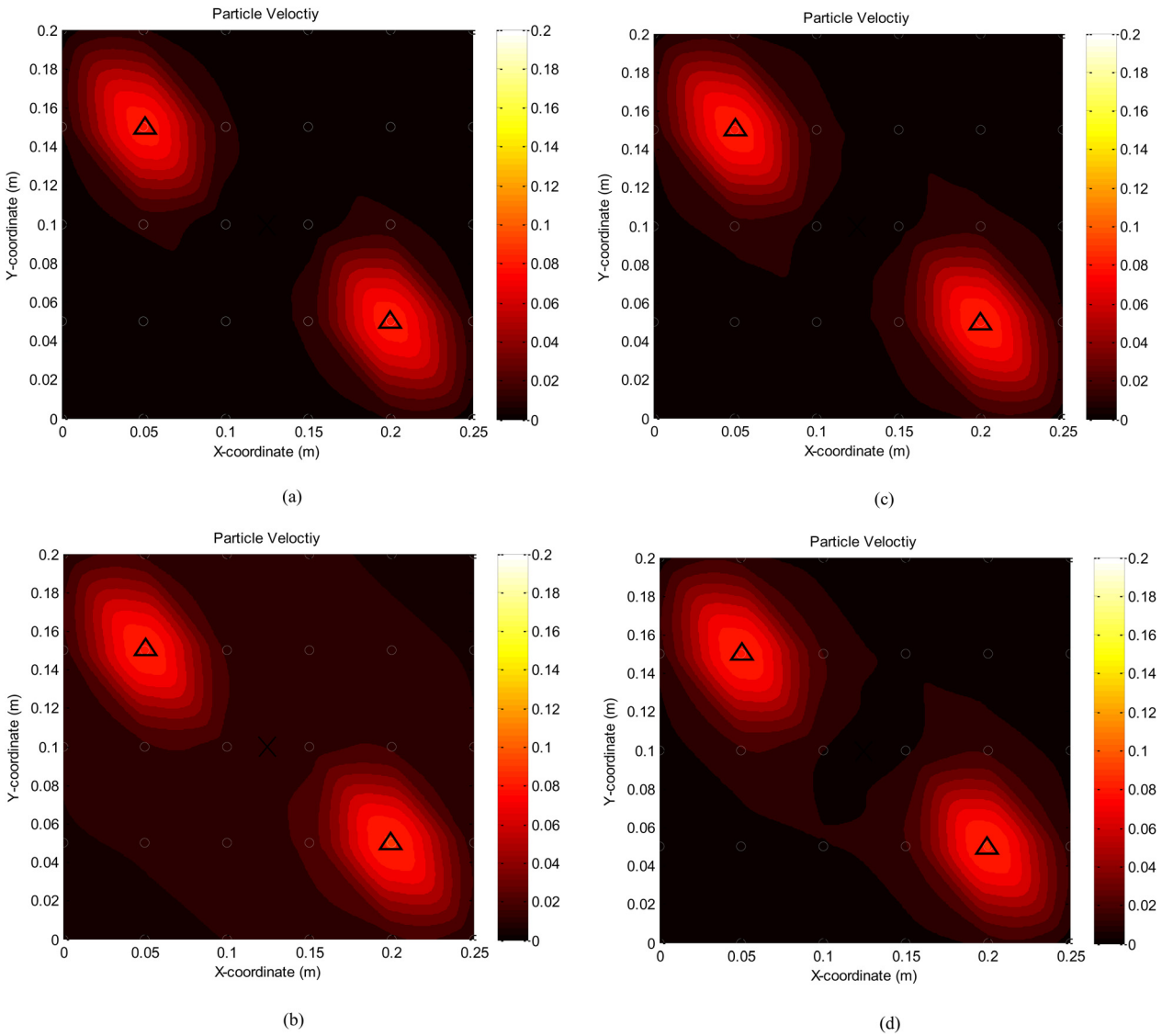

FIG. 9. (Color online) Simulation of the velocity image reconstructed by the ESM-NAH using (a) *p*-based array, (b) *u*-based array, (c) *pu*-based array, and (d) optimal array. Two target sources and the interfering source at the center placed 0.1 m behind the microphone array is indicated (source: Δ, interferer: ×).

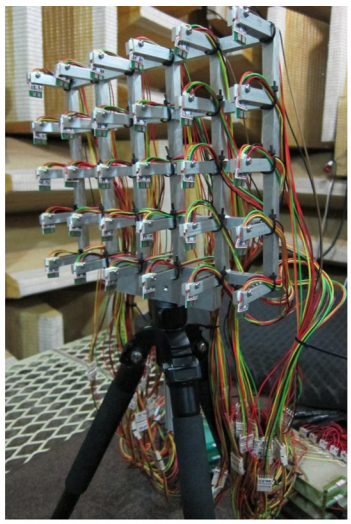

(a)

(b)

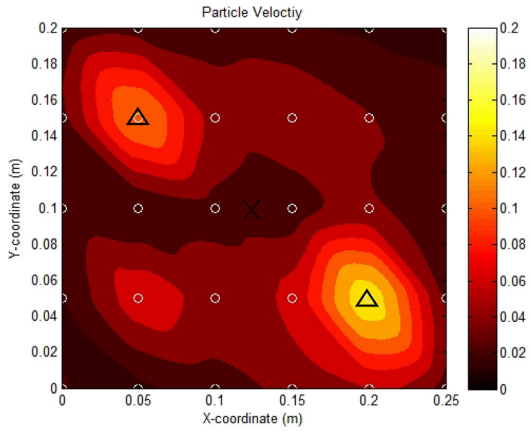

(c)

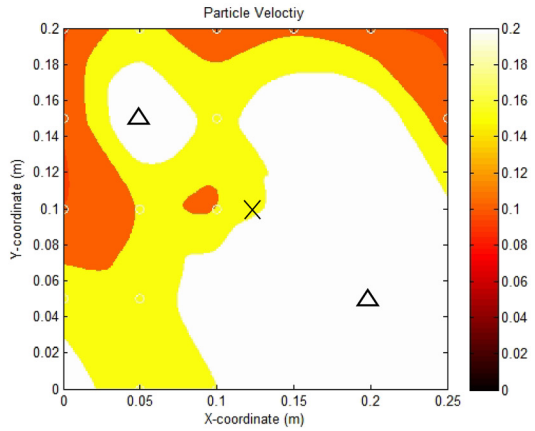

(d)

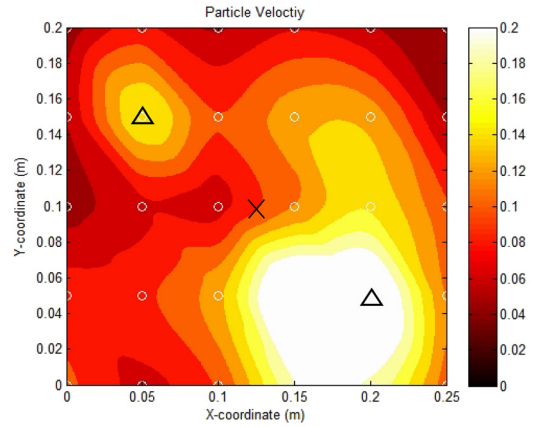

(e)

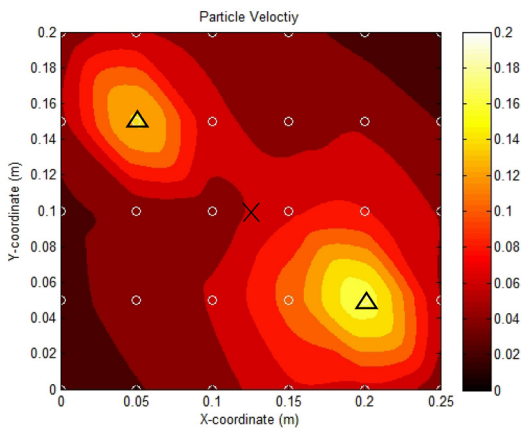

(f)

FIG. 10. (Color online) Experiment of surface velocity reconstruction by the ESM-NAH. (a) Construction of the miniature MEMS directional array, (b) the loudspeaker used as the target sources and the interferer, (c) velocity reconstructed by the *p*-based method, (d) velocity reconstructed by the *u*-based method, (e) velocity reconstructed by the *pu*-based method, and (f) velocity reconstructed by the optimal array. Two target sources and the interfering source at the center that is placed 0.1 m behind the microphone array is indicated (source: Δ, interferer: ×).

IV. CONCLUSIONS

In this work, a two-layer directive microphone array has been developed for NAH applications. Unidirectional microphones are installed in each channel of the array such that the performance of inverse reconstruction can be enhanced without being compromised by interfering sources. Issues regarding channel directional performance and robustness against noise, in comparison with a previous research, are examined. As indicated in the simulation, the

numerical noise in finite difference estimation of particle velocity can nullify the advantage of the well-conditioned velocity-based reconstruction. Performance measures DI and WNG (or coefficient norm) are trade-offs. Channel array filters have been designed, with the aid of a linear quadratic optimization technique. In the proposed approach, the characteristics of each array channel consisting of two microphones are tailored by taking into account not only the directivity (DI) but also the robustness against self-noise (WNG). An objective function based on directivity index and WNG is exploited in the design of an optimal two-element end-fire array.

The proposed optimal array is validated in conjunction with the ESM-based NAH through numerical simulations, with an interfering source positioned behind the array. The results have shown the directive optimal array has yielded significantly improved quality of images in comparison with the previous approaches including the *p*-based method, the *u*-based method and the *pu*-based method, in the presence of an interfering source and sensor noise.

ACKNOWLEDGMENT

The work was supported by the National Science Council (NSC) in Taiwan, Republic of China, under Project No. NSC100-2221-E-007-016-MY3.

[1]V. Murino, "Reconstruction and segmentation of underwater acoustic images combining confidence information in MRF models," J. Pattern Recognit. Soc. **34**, 981–997 (2001).
[2]Y. Fan, B. Tysoe, J. Sim, K. Mirkhani, A. N. Sinclair, F. Honarvar, H. Sildva, A. Szecket, and R. Hardwick, "Nondestructive evaluation of explosively welded clad rods by resonance acoustic spectroscopy," Ultrasonics **41**, 369–375 (2003).
[3]U. Benko, J. Petrovcic, D. Juricic, J. Tavcar, J. Rejec, and A. Stefanovska, "Fault diagnosis of a vacuum cleaner motor by means of sound analysis," J. Sound Vib. **276**, 781–806 (2004).
[4]V. Martin, T. Le Bourdon, and A. M. Pasqual, "Numerical simulation of acoustic holography with propagator adaptation, application to a 3D disc," J. Sound Vib. **330**, 4233–4249 (2011).
[5]E. G. Williams and J. D. Maynard, "Holographic imaging without the wavelength limit," Phys. Rev. Lett. **45**, 554–557 (1980).
[6]B. D. Van Veen and K. M. Buckley, "Beamforming: A versatile approach to spatial filtering," IEEE ASSP Mag. **5**, 4–24 (1998).
[7]H. Krim and M. Viberg, "Two decades of array signal processing research," IEEE Signal Process. Mag. **13**, 67–94 (1996).
[8]J. Hald, "Non-stationary STSF," Technical Review No. 1, Brüel & Kjær, Nærum, Denmark, 2000, pp. 1–36.
[9]W. A. Veronesi and J. D. Maynard, "Digital holographic reconstruction of sources with arbitrarily shaped surface," J. Acoust. Soc. Am. **85**, 588–598 (1988).
[10]M. R. Bai, "Application of BEM (boundary element method)-based acoustic holography to radiation analysis of sound sources with arbitrarily shaped geometries," J. Acoust. Soc. Am. **92**, 533–549 (1992).
[11]B. K. Kim and J. G. Ih, "On the reconstruction of vibro-acoustic field over the surface enclosing an interior space using the boundary element method," J. Acoust. Soc. Am. **100**, 3030–3016 (1996).
[12]S. C. Kang and J. G. Ih, "Use of non-singular boundary integral formulation for reducing errors due to near-field measurements in the boundary element method based near-field acoustic holography," J. Acoust. Soc. Am. **109**, 1320–1328 (2001).
[13]N. P. Valdivia, E. G. Williams, and J. Klos, "Reconstruction of the acoustic field using a conformal array," *Proceedings of Inter-Noise*, December 3–6, 2006, Honolulu, HI.
[14]J. Hald and J. Gomes, "A comparison of two patch NAH methods," *Proceedings of Inter-Noise*, December 3–6, 2006, Honolulu, HI.
[15]S. F. Wu, "On reconstruction of acoustic pressure fields using the Helmholtz equation least squares method," J. Acoust. Soc. Am. **107**, 2511–2522 (2000).
[16]A. Sarkissian, "Method of superposition applied to patch near-field acoustical holography," J. Acoust. Soc. Am. **118**, 671–678 (2005).
[17]J. Gomes, J. Hald, P. Juhl, and F. Jacobsen, "On the applicability of the spherical wave expansion with a single origin for near-field acoustical holography," J. Acoust. Soc. Am. **125**, 1529–1537 (2009).
[18]P. A. Nelson and S. H. Yoon, "Estimation of acoustic source strength by inverse methods: Part I, conditioning of the inverse problem," J. Sound Vib. **233**, 643–668 (2000).
[19]P. A. Nelson and S. H. Yoon, "Estimation of acoustic source strength by inverse methods: Part II, experimental investigation of methods for choosing regularization parameters," J. Sound Vib. **233**, 669–705 (2000).
[20]M. R. Bai and J. H. Lin, "Source identification system based on the time-domain nearfield equivalence source imaging: Fundamental theory and implementation," J. Sound Vib. **307**, 202–225 (2007).
[21]M. R. Bai and J. H. Lin, "A new noise source identification technique: Nearfield acoustical beamformer (NABF)," *Proceedings of Inter-Noise*, December 3–6, 2006, Honolulu, HI.
[22]M. R. Bai and J. H. Lin, "Sound field reconstruction using the time-domain nearfield equivalence source imaging (NESI) technique," *Proceedings of Inter-Noise*, August 28–31, 2007, Istanbul, Turkey.
[23]E. G. Williams, *Fourier Acoustics* (Academic, New York, 1999), pp. 1–296.
[24]S. F. Wu, "Methods for reconstructing acoustic quantities based on acoustic pressure measurements," J. Acoust. Soc. Am. **124**, 2680–2697 (2008).
[25]F. Jacobsen and Y. Liu, "Near field acoustic holography with particle velocity transducers," J. Acoust. Soc. Am. **118**, 3139–3144 (2005).
[26]Y.-B. Zhang, F. Jacobsen, C.-X. Bi, and X.-Z. Chen, "Near field acoustic holography based on the equivalent source method and pressure-velocity transducers," J. Acoust. Soc. Am. **126**, 1257–1263 (2009).
[27]F. Jacobsen and H. E. de Bree, "A comparison of two different sound intensity measurement principle," J. Acoust. Soc. Am. **118**, 1510–1517 (2005).
[28]S. L. Gay and J. Benesty, *Acoustic Signal Processing for Telecommunication* (Kluwer Academic, Norwell, MA, 2000), pp. 181–236.
[29]D. Stanzial, G. Sacchi, and G. Schiffrer, "Calibration of pressure-velocity probes using a progressive plane wave reference field and comparison with nominal calibration filters," J. Acoust. Soc. Am. **129**, 3745–3755 (2011).
[30]H. Teutsch and G. W. Elko, "First-and second-order adaptive differential microphone arrays," *International Workshop on Acoustic Echo and Noise Control*, Darmstadt, Germany, 2001, pp. 35–38.
[31]M. Brandstein and D. Ward (Eds.), *Microphone Arrays* (Springer, New York, 2001), pp. 19–38.
[32]H. L. Van Trees, *Optimum Array Processing* (Wiley, New York, 2002), pp. 59–66.
[33]M. R. Bai, C. C. Chen, and J. H. Lin, "On optimal retreat distance for the equivalent source method-based nearfield acoustical holography," J. Acoust. Soc. Am. **92**, 1407–1416 (2011).
[34]R. Jeans and I. C. Mathews, "The wave superposition method as a robust technique for computing acoustic fields," J. Acoust. Soc. Am. **92**, 1156–1166 (1992).
[35]E. Kreyszig, *Advanced Engineering Mathematics* (Wiley, New York, 2006), pp. 798–801.